



Defining megathrust tsunami source scenarios for northernmost Cascadia

Dawei Gao¹ · Kelin Wang^{1,2}  · Tania L. Insua³ · Matthew Sypus¹ · Michael Riedel⁴ · Tianhaozhe Sun⁵

Received: 21 December 2017 / Accepted: 13 June 2018 / Published online: 2 July 2018
© Crown 2018

Abstract

For assessing tsunami hazard in northernmost Cascadia, there is an urgent need to define tsunami sources due to megathrust rupture. Even though the knowledge of Cascadia fault structure and rupture behaviour is limited at present, geologically and mechanically plausible scenarios can still be designed. In this work, we use three-dimensional dislocation modelling to construct three types of rupture scenarios and illustrate their effects on tsunami generation and propagation. The first type, buried rupture, is a classical model based on the assumption of coseismic strengthening of the shallowest part of the fault. In the second type, splay-faulting rupture, fault slip is diverted to a main splay fault, enhancing seafloor uplift. Although the presence or absence of such a main splay fault is not yet confirmed by structural observations, this scenario cannot be excluded from hazard assessment. In the third type, trench-breaching rupture, slip extends to the deformation front and breaks the seafloor by activating a frontal thrust. The model frontal thrust, based on information extracted from multichannel seismic data, is hypothetically continuous along strike. Our low-resolution tsunami simulation indicates that, compared to the buried rupture, coastal wave surface elevation generated by the splay-faulting rupture is generally 50–100% higher, but that by trench-breaching rupture is slightly lower, especially if slip of the frontal thrust is large (e.g. 100% of peak slip). Wave elevation in the trench-breaching scenario depends on a trade-off between enhanced short-wavelength seafloor uplift over the frontal thrust and reduced uplift over a broader area farther landward.

Keywords Tsunami sources · Cascadia subduction zone · Megathrust earthquakes · Splay-faulting rupture · Trench-breaching rupture · Dislocation modelling

✉ Kelin Wang
kelin.wang@canada.ca

¹ School of Earth and Ocean Sciences, University of Victoria, Victoria, BC, Canada

² Pacific Geoscience Centre, Geological Survey of Canada, Sidney, BC, Canada

³ Ocean Networks Canada, University of Victoria, Victoria, BC, Canada

⁴ GEOMAR Helmholtz Centre for Ocean Research, Kiel, Germany

⁵ Department of Geosciences, Pennsylvania State University, University Park, PA, USA

1 Introduction

Great megathrust earthquakes have not occurred along the Cascadia margin over its approximately two century's recorded history, but paleoseismic evidence (Atwater et al. 1995; Goldfinger et al. 2012) indicates that these events repeatedly occurred in the past. The last great Cascadia earthquake ($M_w \sim 9$) occurred on 26 January, AD 1700, and generated a powerful tsunami that probably caused serious damage along the Cascadia coast (Ludwin et al. 2005). The tsunami also caused damage along the Japanese coast across the Pacific (Satake et al. 2003). The west coast of North America is under the threat of future great megathrust earthquakes and the associated tsunamis (Leonard et al. 2012). For tsunami hazard assessment, various realistic rupture scenarios need to be considered (Fig. 1).

The main objective of this paper is to address an urgent need in tsunami hazard assessment at northernmost Cascadia including southern Vancouver Island and the explorer segment north of the Nootka fault zone (NFZ) (Fig. 2). Earlier near-uniform-slip models such as those used by Satake et al. (2003) and Cherniawsky et al. (2007) are adequate for modelling the impact of a Cascadia tsunami across the Pacific or for illustrating the potential impact on the Cascadia coast to the first order. Existing megathrust tsunami source models that are of sufficient resolution for local coastal tsunami hazard

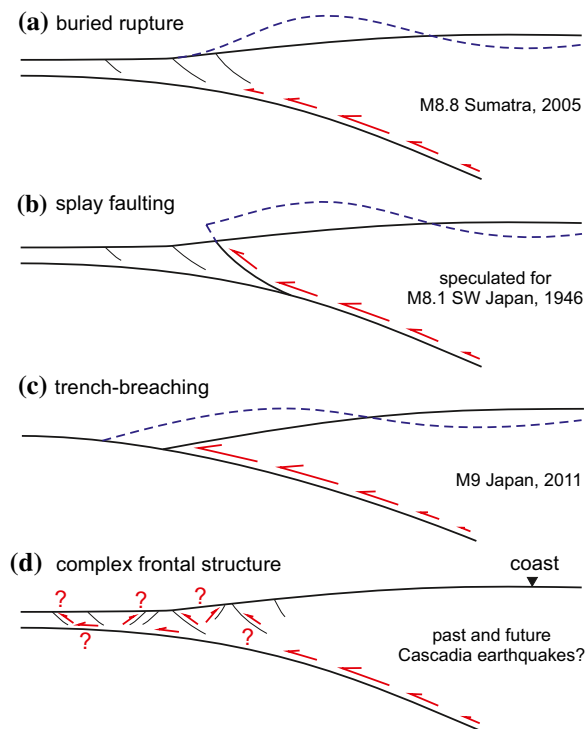
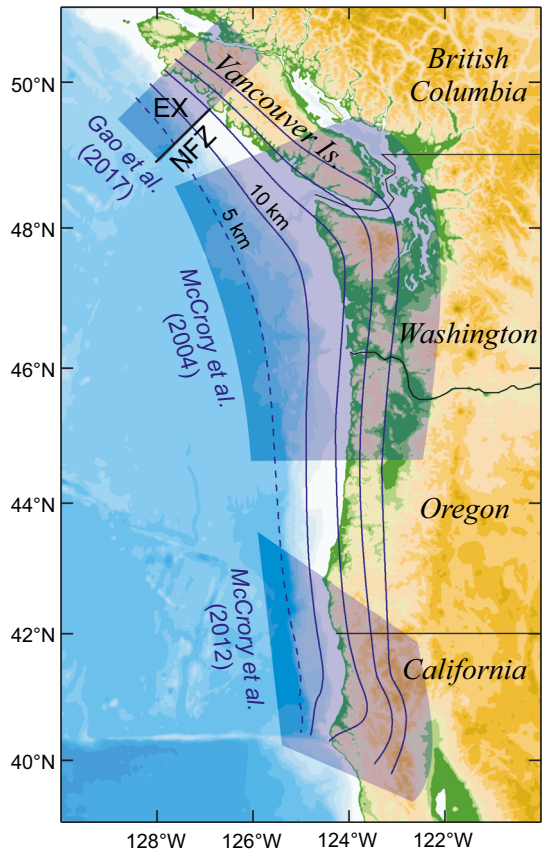


Fig. 1 Four rupture scenarios of subduction zone earthquakes for generating tsunamis (Wang and Tréhu 2016). Red arrows represent coseismic slip. Dashed lines represent coseismically deformed seafloor. **a** Buried rupture, **b** splay-faulting rupture, **c** trench-breaching rupture, **d** activation of thrusts and back-thrusts

Fig. 2 New megathrust geometry model for Cascadia based on McCrory et al. (2004), McCrory et al. (2012) and Gao et al. (2017). Smooth along-strike transition is assumed between the shaded areas. Depth to the plate interface is contoured in 10 km increments (solid lines) except for the 5 km contour (dashed). *NFZ* Nootka fault zone, *EX* explorer segment



assessment are focused on the Oregon part of the margin (e.g. Priest et al. 2009, 2010; Witter et al. 2011, 2013).

For the Oregon part of the Cascadia margin, two types of megathrust tsunami source have been assumed (e.g. Priest et al. 2009, 2010; Witter et al. 2012, 2013): buried rupture (Fig. 1a) and splay faulting (Fig. 1b). However, the 2011 M_w 9.0 Tohoku-oki earthquake raised a new question (Wang and Tréhu 2016). Cross-trench bathymetric and seismic observations before and after the earthquake (Fujiwara et al. 2011; Kodaira et al. 2012; Sun et al. 2017) indicate that large coseismic slip extended to the trench axis, responsible for a devastating tsunami (Fig. 1c). Therefore, in this work, we not only develop scenarios of buried and splay-faulting ruptures, but also investigate the possibility of trench-breaching rupture and develop relevant source models. We make an effort to improve existing tsunami source models for the whole Cascadia margin by using an updated megathrust geometry, even though our geographic focus is northernmost Cascadia.

Source definition is only one step, albeit a critically important step, in mitigating tsunami risk due to local megathrust earthquakes. What we report in this paper is focused mainly on one component of the source definition, that is, slip distribution in the dip direction and the associated involvement of secondary faults (Fig. 1). It is our hope that the rupture scenarios presented in this paper and their future more refined versions will enable the development of more comprehensive source models and tsunami inundation models to

guide the design of mitigation strategy. The inundation models can also be used for the development of a tsunami early warning system. Insights from this study can be applied to other subduction zones where great subduction zone earthquakes and their tsunamis pose threat, but have not been instrumentally recorded.

2 Fault geometry and modelling method

2.1 Cascadia megathrust geometry

For our tsunami source modelling, we compiled a new geometrical model for the Cascadia megathrust. The new geometry is based on a combination of three parts (Fig. 2). For southernmost Cascadia, the fault geometry is taken directly from McCrory et al. (2012) which is based primarily on precise relocation of Wadati–Benioff (WBZ) earthquakes using the double-difference method. It features a more complex geometry than earlier models in this area. For northern and central Cascadia from southern Vancouver Island to central Oregon, we adopt the geometry proposed earlier by McCrory et al. (2004) on the basis of wide-angle seismic reflection and refraction data for the shallow part and tele-seismic travel time data and intraslab earthquake hypocentres for the deeper part. For this area, we do not use the newer model of McCrory et al. (2012) because it depicts buckling of the subducting slab at rather short wavelengths that is not convincingly supported by observations. We assume a smooth spatial transition between the two models (Fig. 2).

Existing geometrical models of the Cascadia megathrust do not include the explorer segment north of the NFZ for lack of observational constraints. However, low-frequency earthquake (LFE) hypocentres located around 35 km depth by Royer and Bostock (2014) have now provided some constraints (Gao et al. 2017). By assuming that the LFEs occur on the plate interface, Gao et al. (2017) devised two candidate two-dimensional fault geometries for the explorer segment which differ in the preciseness of fitting the LFEs. For the shallowest offshore part where tsunamigenic ruptures can initiate and propagate, the difference between these two candidate models is very small. Here, we extrapolate from the simpler one, which features monotonically increasing dip with depth, to construct a three-dimensional (3D) geometrical model for the explorer segment (Fig. 2). A smooth geometrical transition is assumed from the explorer segment to southern Vancouver Island (Fig. 2), although it is possible that the downdip extension of the NFZ may cause a sharp change in the fault geometry.

For validation purposes, we used the new megathrust geometry to re-examine the heterogeneous fault slip distribution of Wang et al. (2013) for the AD 1700 great Cascadia earthquake that features four high-slip patches separated by low-slip areas. Wang et al.'s (2013) model was constrained by coseismic coastal subsidence estimated from microfossil data and was constructed using the megathrust geometry of McCrory et al. (2004). We mapped the slip vectors of Wang et al. (2013) onto our new fault geometry. In terms of coastal subsidence, the results using the new fault geometry, shown in Gao (2016), are nearly identical to those of Wang et al. (2013) and therefore are not displayed here.

2.2 Dislocation model

We design tsunami sources with a 3D dislocation model in a uniform elastic half-space. The Poisson's ratio is assumed to be 0.25; no other elastic modulus is needed for the uniform half-space. Compared to uncertainties in coseismic slip magnitude and

distribution, the effects of heterogeneous material properties such as rigidity are very minor issues. Our computer code numerically integrates the point-source dislocation solution (Green’s function) of Okada (1985) over a 3D megathrust and yields displacement values on the surface of the model (Fig. 3a). Okada (1985, 1992) had analytically integrated the point-source solution to obtain a solution for a uniform-slip, planar rectangular fault. Here, we do the integration numerically because of our curved fault geometry and spatially variable slip. The code has been extensively benchmarked and applied to earthquake modelling (e.g. Wang et al. 2003, 2013; Priest et al. 2010).

For the numerical integration, the fault is divided into triangular integration elements each representing a point source (Flück et al. 1997; Wang et al. 2003). Deformation at the surface is thus the sum of the contributions from all the point sources. An uneven element size distribution can be used if we need extremely high mesh density in only limited areas of the fault such as where the rupture breaches the surface (seafloor) in the splay-faulting and trench-breaching models.

For the accuracy of numerical integration, one generally should avoid calculating deformation at locations very close to the fault. This becomes an issue near the trace of a splay or trench-breaching fault. Here, the fault depth approaches zero, so that seafloor deformation needed by tsunami modelling has to be calculated at short distances above the dipping fault. For this reason, we use very small fault triangles (300–350 m in both the strike and dip dimensions) near the fault trace and derive deformation of the hanging-wall side of the seafloor at distances 1600 m or greater from the fault trace. The foot-wall side is less affected, and the minimum distance used is 160 m. The 1760 m “gap” along the fault trace adequately approximates the deformation discontinuity across the fault trace.

Because the dislocation model for our source construction assumes a flat free surface, it cannot directly account for the presence of the continental slope. To overcome this

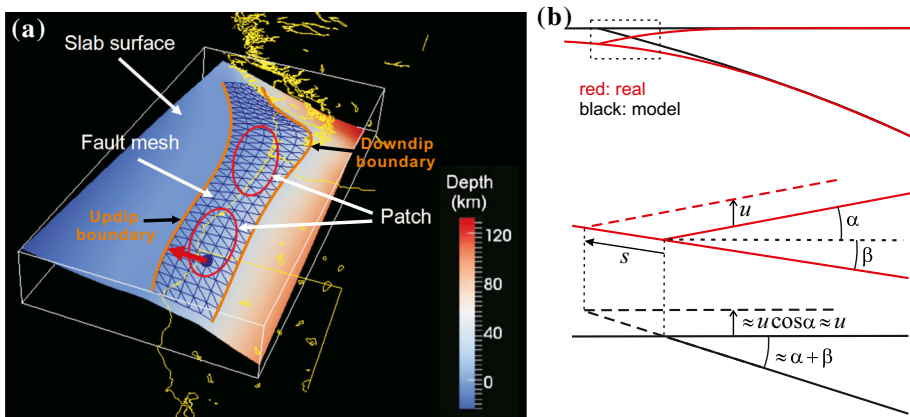


Fig. 3 Dislocation model. **a** Schematic illustration of the fault mesh for Cascadia [modified from Wang (2012)]. Coastlines and political boundaries are shown in yellow. Very large triangular elements are shown here to illustrate the concept. The triangles actually used for numerical integration are much smaller. In particular, meshes for the splay fault and frontal thrust are very dense near the updip edge with element dimensions of a few 100 m. **b** Schematic illustration of the fault dip adjustment to compensate for the effect of not having a sloping seafloor in the flat-top dislocation model [modified from Wang et al. (2018)]. The dotted box in the upper panel outlines the trench area shown in the lower panel which illustrates trench-breaching rupture. In the lower panel, solid and dashed lines represent the seafloor position before and after, respectively, fault slip s takes place, and u is the resultant seafloor rise relative to seawater

problem, we make a slight adjustment to the shallowest part of the megathrust fault. Following previous work (Flück et al. 1997; Wang et al. 2003, 2013), we reduce the depths of the shallow part of the fault so that the fault depth below the free surface in the model approximately corresponds to the fault depth below seafloor in reality (Fig. 3b). This adjustment is not very important for modelling buried ruptures, but is critically important for modelling trench-breaching ruptures (Wang et al. 2018). Assuming seafloor slope angle α , fault dip β , and trench-breaching fault slip s , the rise of the near-trench seafloor is $u = s \sin(\alpha + \beta) / \cos(\alpha)$ (Fig. 3b). With the fault dip adjustment in a flat-surface model as shown in Fig. 3b, Wang et al. (2018) have shown that the near-trench seafloor rise due to the same fault slip is $u' \approx s \sin(\alpha + \beta) \approx u$ (Fig. 3b). In other words, what is lost by not having a seafloor slope in the flat-surface model is compensated by the greater vertical seafloor displacement due to the larger fault dip.

We determine directions of fault slip vectors using Euler vectors in exactly the same way as in Wang et al. (2003). The direction of coseismic slip is assumed to be along the convergence direction between the Juan de Fuca plate and the Cascadia forearc (Wang et al. 2003). The motion of the forearc area with respect to stable North America, based on the model of Wells and Simpson (2001), affects central and southern Cascadia, but has little effect on our region of interest. Although other forearc motion models are available, uncertainties in individual models are probably larger than differences between models (Wang and Tréhu 2016). The product of an equivalent time (in years) of slip deficit accumulation and the local subduction rate, which varies gradually along strike, can be used to define slip magnitude. The spatial distribution of the slip magnitude differs between different rupture scenarios and will be described in the ensuing sections.

For the explorer segment, the downdip rupture limit was proposed by Gao et al. (2017) based on thermal modelling. For the rest of Cascadia, the downdip limit was proposed by Wang et al. (2003) based on similar arguments. For southernmost Cascadia, we have slightly modified the downdip limit of Wang et al. (2003) to accommodate the more complex shape of the new megathrust geometry discussed in Sect. 2.1.

Given fault slip, the size of an earthquake is measured using the moment magnitude (Hanks and Kanamori 1979):

$$M_w = \log_{10}(M_0 - 9.05) / 1.5, \quad (1)$$

where M_0 is the scalar seismic moment in N m, which is the product of shear modulus, rupture area, and average fault slip. Because the focus of this paper is mainly slip distribution in the dip direction and related activation of secondary faults, we do not address other aspects of megathrust tsunami source definition such as maximum earthquake magnitude or slip distance and recurrence behaviour. These other aspects may require considering various statistically derived scaling relationships that describe how M_w or M_0 scales with rupture length, width, or area (e.g. Wells and Coppersmith 1994), especially those specific to subduction megathrusts (Blaser et al. 2010; Strasser et al. 2010; Murotani et al. 2013; Allen and Hayes 2017). However, defining the scaling relationships for very large earthquakes is very difficult because of the very small sample base.

Of greater importance is the question whether the scaling relationships constrained by smaller events can be extrapolated to giant events. Strasser et al. (2010) showed that rupture width appears to saturate at around 200 km for $M_w > 8.7$, an observation consistent with the notion of a rheologically controlled downdip limit of megathrust rupture. Wang et al. (2018) pointed out the dramatic contrast between the M_w 9.0 2011 Tohoku-oki and the M_w 9.2 2004 Sumatra ruptures, with the former being very compact (short length,

huge slip), but the latter very spread out (huge length, moderate slip), representing two end-member types of giant megathrust earthquakes. Because Cascadia is similar to northern Sumatra in terms of large amounts of trench sediment and consequently smooth plate interface (Wang and Tréhu 2016), there is reason to expect its great megathrust earthquake to be of the Sumatra type.

2.3 Grouping and naming of rupture models

In Sect. 3, we will describe 15 rupture models as potential tsunami sources (Table 1). This by no means constitutes a complete suite for tsunami hazard assessment, but serves to guide future more refined models. By assuming different slip behaviour of the shallowest part of the fault, we devise three categories of rupture scenarios (indicated by the first letter of their names): buried rupture (B-models), splay-faulting rupture (S-models), and trench-breaching rupture (T-models), which can be considered the Cascadia version of what is illustrated in Fig. 1a–c, respectively. The splay-faulting category is subdivided into two groups, A and B, having different splay-fault geometry, and the trench-breaching category is subdivided into two groups with fault slip at the deformation front being 50 and 100% of assigned peak slip of the rupture (Table 1).

Based on thermal arguments and limited geodetic evidence for fault locking, the explorer segment of the northernmost Cascadia subduction zone (Fig. 2) is inferred to be capable of producing tsunamigenic megathrust earthquakes (Gao et al. 2017). But there is uncertainty whether the explorer segment would rupture independently or together with the rest of the megathrust. We therefore consider three strike-length groups corresponding to the three columns in Table 1. The suffix at the end of each model name in Table 1 indicates the model's strike-length group. The map view of the three strike lengths is shown in Fig. 4a; other details of the models shown in Fig. 4a will be discussed in Sect. 3.1.

In strike-length group EX, the explorer segment (EX) north of the Nootka fault ruptures independently. In group NoEX, the rupture is along the entire Cascadia margin without the EX. Group Whole is a combination of groups EX and NoEX. Dividing NoEX into shorter segments can result in many other possible scenarios. For example, a segment can be defined between the Nootka fault and a southern boundary roughly corresponding to a

Table 1 Summary of rupture scenarios for tsunami hazard assessment

| | EX | NoEX | Whole |
|------------------------------------|------------------------|--------------------------|---------------------------|
| Buried rupture | B-EX (Fig. 4a) | B-NoEX (Fig. 4a) | B-Whole (Fig. 4a) |
| Splay-faulting rupture A | S-A-EX (Fig. 6a) | S-A-NoEX (Fig. 6a) | S-A-Whole (Fig. 6a) |
| Splay-faulting rupture B | S-B-EX (Fig. 6c) | S-B-NoEX (Fig. 6c) | S-B-Whole (Fig. 6c) |
| Trench-breaching 50% of peak slip | T-50-EX (Fig. 11a) | T-50-NoEX (Fig. 11a) | T-50-Whole (Fig. 11a) |
| Trench-breaching 100% of peak slip | T-100-EX (Fig. 11c) | T-100-NoEX (Fig. 11c) | T-100-Whole (Fig. 11c) |

EX explorer segment alone, *NoEX* Cascadia megathrust without EX, *Whole* whole-margin rupture (combination of EX and NoEX; see Fig. 4a)

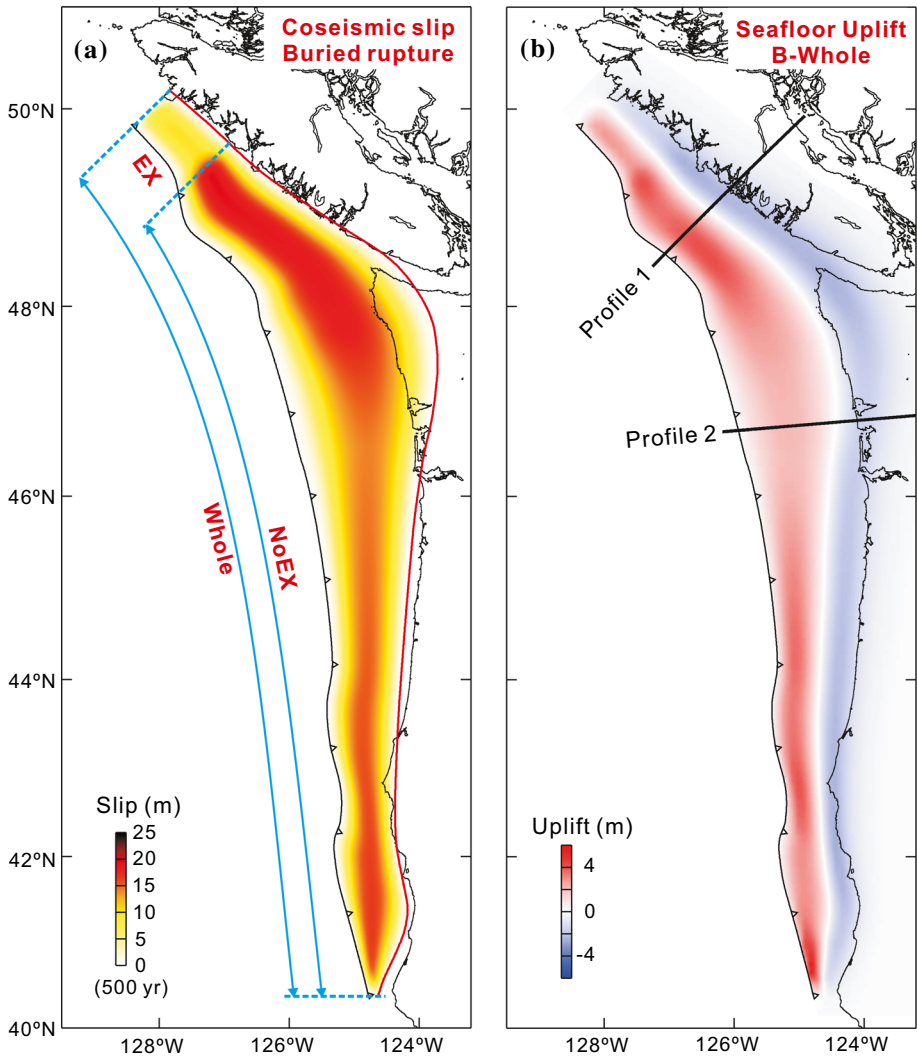


Fig. 4 Buried-rupture scenarios. Barbed black line shows the deformation front. **a** Coseismic fault slip distribution of four buried-rupture scenarios. Solid red line marks the downdip limit of coseismic slip. Southern boundary of scenario B-Ex corresponds to the Nootka fault. **b** Seafloor uplift and coastal subsidence induced by scenarios B-Whole. Results along the two profiles are shown in Fig. 5

segment boundary between latitudes 45° and 46° as inferred from turbidite records (Goldfinger et al. 2012) which is also a low-slip area during the AD 1700 earthquake inferred from coastal subsidence estimates based on microfossil observations (Wang et al. 2013). It may rupture by itself or together with EX.

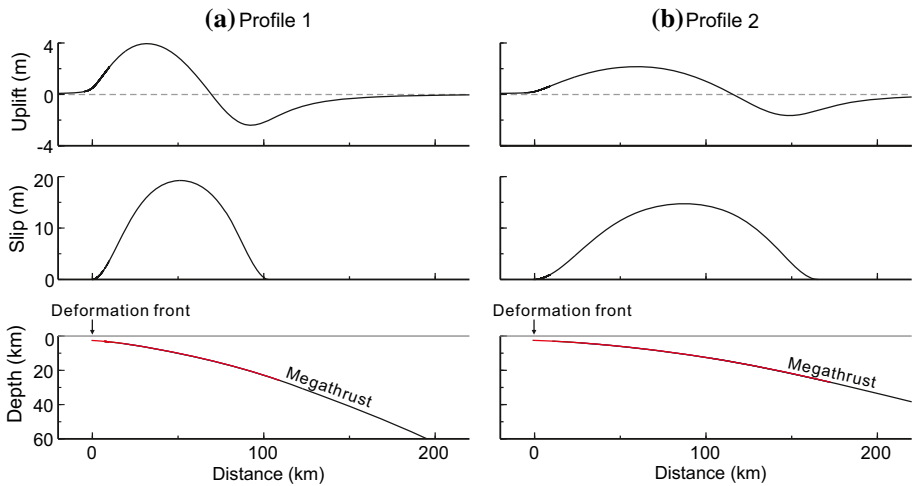


Fig. 5 Fault slip and surface deformation along the two profiles shown in Fig. 4b for buried-rupture scenario B-Whole. For each profile, the bottom panel shows the fault geometry with the red portion indicating the rupture zone, the middle panel shows fault slip distribution which follows the bell-shaped function of Eq. (2) with $p = 0.2$ and $q = 0.5$, and the upper panel shows seafloor uplift

3 Megathrust tsunami sources

3.1 Buried rupture

The buried-rupture scenario (Fig. 1a) is based on the assumption that the shallowest portion of the megathrust exhibits a velocity-strengthening behaviour which normally resists seismic slip during an earthquake, but allows aseismic slip after the earthquake (e.g. Wang and Hu 2006). An example is the 28 March 2005 M_w 8.7 Nias earthquake, Sumatra. Continuous Global Positioning System observations on forearc islands (~ 60 km from the trench) detected little slip of the shallow portion of the fault during the earthquake but significant aseismic slip afterwards (Hsu et al. 2006; Sun and Wang 2015).

The following bell-shaped function describing the downdip slip distribution in a buried rupture was proposed by Wang and He (2008), with typos corrected in Wang et al. (2013),

$$s(x') = s_0 \delta(x') \left\{ 1 + \sin \left[\pi \delta(x')^b \right] \right\} \tag{2a}$$

$$\delta(x') = \begin{cases} \frac{6}{q^3} x'^2 \left(\frac{q}{2} - \frac{x'}{3} \right) & 0 \leq x' \leq q \\ \frac{6}{(1-q)^3} (1-x')^2 \left(\frac{1-q}{2} - \frac{1-x'}{3} \right) & q \leq x' \leq 1 \end{cases}, \tag{2b}$$

where $x' = x/w$ is the ratio of the downdip distance x from the upper limit of the rupture zone to the downdip width w of the rupture zone, s_0 is peak slip, b is a broadness parameter ranging from 0 to 0.3, and q is a skewness parameter ranging from 0 to 1. A symmetric distribution with $b = 0.2$ and $q = 0.5$ has been applied in a number of studies (e.g. Priest et al. 2009, 2010, 2013, 2014; Wang et al. 2013; Witter et al. 2011, 2012, 2013) for

megathrust rupture modelling at Cascadia and is also used for all the buried-rupture models in this work.

We assign 500 years of slip deficit to the apex of the bell-shaped distribution in all the models (Fig. 4). Since great megathrust earthquakes occur at Cascadia about every 500 years on average (Goldfinger et al. 2012), it is convenient to use this number here. Because seafloor deformation is proportional to fault slip, the results can be readily scaled to obtain deformation due to other slip values. The peak slip varies along strike because of variations in the subduction rate. Results along two margin-normal profiles (Fig. 4b) are shown in Fig. 5.

Seafloor deformation for B-Whole, a combination of B-EX and B-NoEX, is shown in Fig. 4b. The rupture results in seafloor uplift and coastal subsidence. An example of tsunami wave propagation induced by model B-Whole is given in Sect. 4.

3.2 Splay-faulting rupture

During a great megathrust earthquake, a splay fault may be activated because of a sudden compression of the outer accretionary wedge if the shallowest portion of the megathrust exhibits coseismic strengthening (Wang and Hu 2006) or because the propagating rupture encounters a stress barrier along the main fault (Wendt et al. 2009). Because of the steeper dip of the splay fault than the megathrust, seafloor uplift will be enhanced (Fig. 1b), contributing to tsunami generation. Splay faulting is suspected to have facilitated tsunami generation in the 1946 Nankai earthquake (Fig. 1b) (e.g. Cummins and Kaneda 2000) and some other great megathrust earthquakes, such as the 1960 Chilean and 1964 Alaskan earthquakes (Plafker 1972). There is indirect structural evidence that a splay fault may be present along the central Cascadia margin, separating older and younger accretionary complexes (Priest et al. 2009). Although the evidence is not conclusive, the possibility of splay faulting cannot be excluded from Cascadia tsunami hazard assessment (see review by Wang and Tréhu 2016).

The inferred splay fault off Washington and Oregon between 45°N and 47°N is in the continental slope near the shelf edge (Priest et al. 2009). Whether and how far it extends northward offshore of Vancouver Island are poorly known. Identification of potential splay faults in available seismic images is so far inconclusive. For tsunami hazard assessment at northernmost Cascadia, we devise two hypothetical splay-fault geometries which both dip $\sim 30^\circ$ landward and sole into the megathrust at depths less than 20 km. In the first one (splay fault A), we merge Priest et al. (2009) fault with the deformation front off Vancouver Island (Fig. 6a), similar to the merging of the splay fault with the deformation front at southern Cascadia assumed in Priest et al. (2009). In the second one (splay fault B), we extend the splay fault proposed for central Cascadia (Priest et al. 2009) northward along the continental shelf edge (Fig. 6c). South of $\sim 47.5^\circ$ N, both these models are identical to the splay-fault model of Priest et al. (2009) except for an updated megathrust geometry. Before further geological information becomes available to confirm the presence or absence of splay faults in this area and their geometry, splay-fault models A and B are useful for exploring how splay faulting might contribute to tsunami generation at northernmost Cascadia.

The two splay-fault geometries give rise to two groups of rupture models whose names begin with S-A and S-B, respectively (Table 1). Similar to the buried-rupture models shown in Fig. 4, each group contains three models of different strike lengths as explained in Sect. 2.3 and shown in Fig. 6a. The fault slip and surface deformation along two profiles

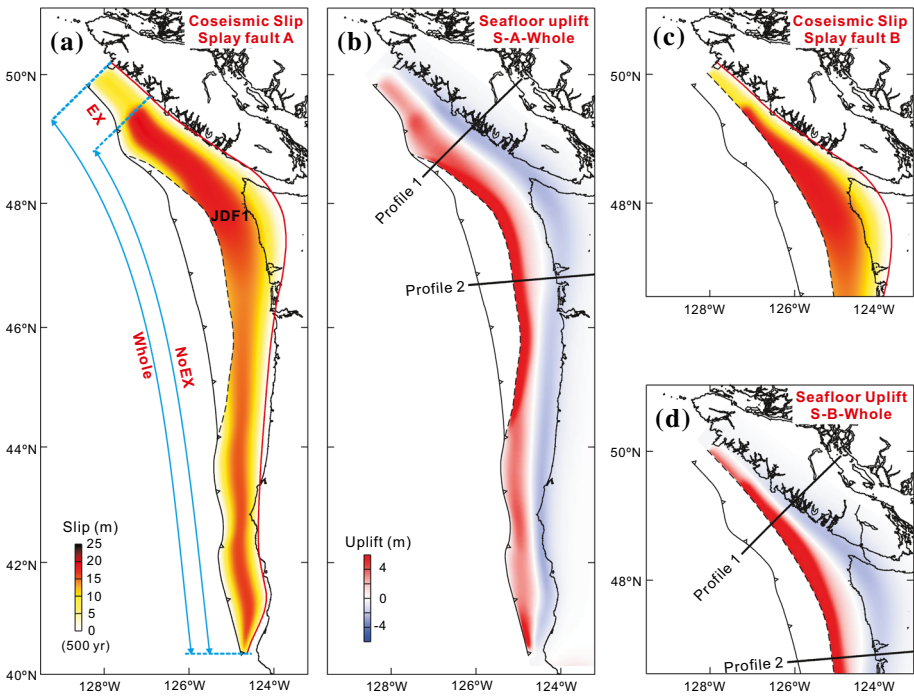


Fig. 6 Splay-faulting rupture scenarios. Black barbed line marks the deformation front; dash line marks the surface trace of the splay fault. Segmentation in the strike direction is the same as in Fig. 4a. Results along the two profiles are shown in Fig. 7. **a** Rupture scenarios with splay-fault geometry group A. Solid red line marks the downdip limit of coseismic slip. **b** Seafloor uplift for model S-A-Whole. **c** Rupture scenario with splay-fault geometry group B. **d** Seafloor uplift for model S-B-Whole. In both **c**, **d** the southern part, being identical to that of group A, is not shown

(Fig. 6b, d) are shown in Fig. 7. For simplicity, the fault slip is assumed to be the buried-rupture slip truncated by the surface trace of the splay fault (Fig. 7). Again, the peak slip value for the models shown in Figs. 6 and 7 is equivalent to 500 years of slip deficit. Given the same peak slip, the splay-fault models can result in seafloor uplift more than twice that of the buried-rupture models (Fig. 5) landward of the seafloor trace of the splay fault but nearly no uplift seaward of it (Fig. 7b). It is important to emphasize that the area of enhanced uplift can extend landward far beyond the point where the splay fault soles into the megathrust. In Sect. 4, a tsunami wave simulation example using source scenario S-A-Whole (Fig. 6b) will show that the splay fault is considerably more potent than the buried rupture in generating tsunamis.

3.3 Trench-breaching rupture

3.3.1 Faulting structure around the deformation front

The possibility of trench-breaching rupture becomes relevant for Cascadia because of the 2011 Tohoku-oki earthquake (Wang and Tréhu 2016). Direct evidence for large coseismic slip breaching the trench during the Tohoku-oki earthquake (Fig. 1c) came from repeat

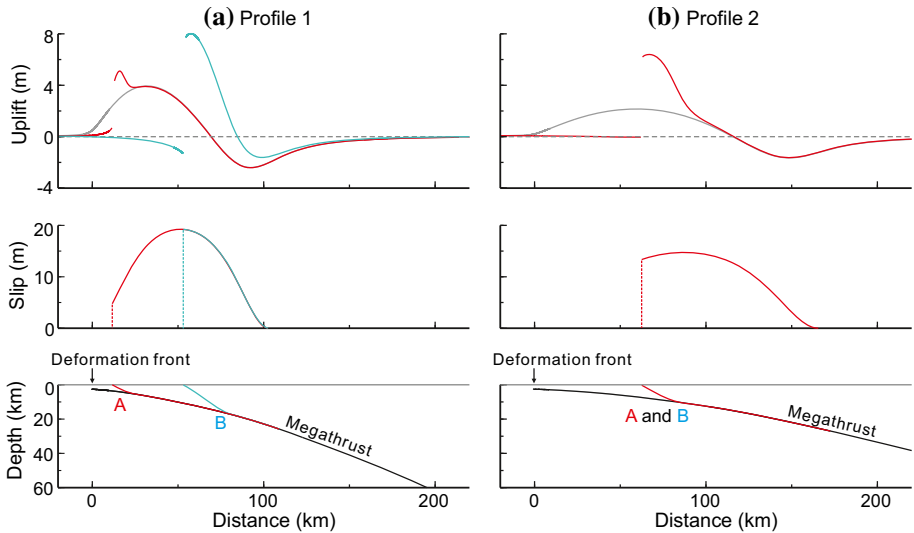


Fig. 7 Fault slip and surface deformation along the two profiles shown in Fig. 6. Those for splay-fault geometry A (Fig. 6b) and B (Fig. 6d) are displayed using red and blue lines, respectively. For each profile, the bottom panel shows the fault geometry with the coloured portion indicating the rupture zone, the middle panel shows fault slip distribution (truncated versions of that in Fig. 5), and the upper panel shows seafloor uplift in comparison with that produced by the buried rupture (grey)

multibeam bathymetry surveys (Fujiwara et al. 2011; Sun et al. 2017) and high-resolution seismic imaging of the trench area (Kodaira et al. 2012) before and after the earthquake.

However, unlike the sediment-starved Japan trench where a continuous décollement extends all the way to the trench, a structure style that facilitates trench-breaching rupture, the trench at northern Cascadia is buried by large amounts of sediment (Fig. 1d). Can the shallowest portion of the Cascadia megathrust coseismically slip to the trench as in the Tohoku-oki earthquake, or would it normally resist coseismic slip but creep aseismically after the earthquake as in the 2005 M_w 8.7 Nias earthquake? Similar to northern Cascadia, the Sumatra trench is also covered by very thick sediment (Gulick et al. 2011). Multiple thrusts and back-thrusts are present in the sediment near the Sumatra trench (Henstock et al. 2006; Singh et al. 2008; Gulick et al. 2011). Seismic (Singh et al. 2011; Gulick et al. 2011; Moeremans et al. 2014) and high-resolution bathymetry (Henstock et al. 2006) studies suggest that secondary faults near the subduction front might have been activated during the 2004 M_w 9.2 Sumatra and 2010 M_w 7.8 Mentawai earthquakes to facilitate coseismic slip to propagate to the trench. If previous megathrust ruptures regularly breached the seafloor at Cascadia, we expect them to have left some signatures in the deformed sediment formation in the deformation front area. With this in mind, we re-examined previously obtained and published seismic imaging data.

Two multichannel seismic surveys were conducted off the west coast of Vancouver Island in 1985 and 1989 by the Geological Survey of Canada (Fig. 8). Data acquisition, processing, and/or interpretation were described by Yorath et al. (1987), Clowes et al. (1987), and Davis and Hyndman (1989) for the 1985 survey and Spence et al. (1991a, b), Hyndman et al. (1994), and Yuan et al. (1994) for the 1989 survey, which represents the best effort of the time. We re-examined reflection images from ten of these profiles (Lines

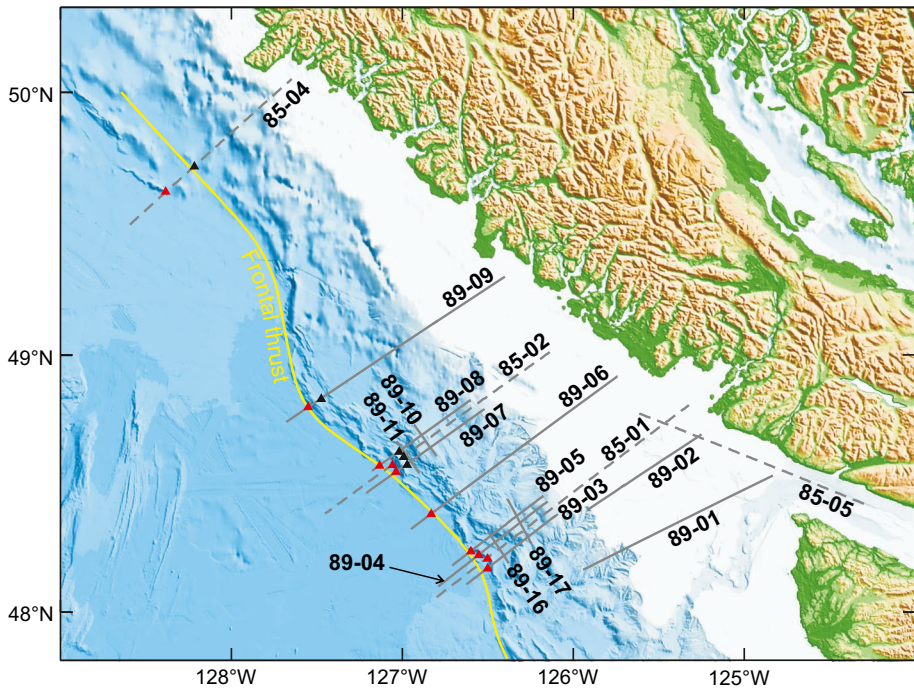


Fig. 8 The 1985 (dashed grey lines) and 1989 (solid grey lines) multichannel seismic reflection survey profiles. Yellow line represents the seafloor trace of our hypothetical frontal thrust for tsunami source modelling. Red and black triangles mark locations where dominant frontal thrusts and back-thrusts, respectively, have been identified

85-01, 85-02, 85-04 and 89-03 through 89-09) in an effort to identify possible secondary thrust faults around the accretionary wedge deformation front.

All the 1985 seismic survey images were presented in terms of both depth and two-way travel time in the original references (Clowes et al. 1987; Davis and Hyndman 1989), but those from the 1989 surveys were presented only in two-way travel time (Spence et al. 1991a; Hyndman et al. 1994) except for Lines 89-04 and 89-07 from Yuan et al. (1994). To obtain deformation structures near the deformation front, it would be ideal to convert the two-way travel time to depth for the other 1989 lines.

Unfortunately, we do not have digital velocity information for these old profiles to do a time–depth conversion in a timely fashion. One strategy would be to take the velocity information from the printed records, hand-edit them into a proper format, and then read them into a computer processing package for the conversion. Another strategy, which we adopt in this work, is to hand-measure the depth and two-way travel time sections of Lines 89-04 and 89-07 from Yuan et al. (1994) to get an approximate “two-way travel time versus depth” relationship to be applied to the other 1989 lines. Given the many assumptions and simplifications in the tsunami source modelling, the second approach is more than adequate for our purpose.

From manually converted depth sections for Lines 89-03, 89-05, 89-06, 89-08, and 89-09 and the original depth sections for the other 5 lines, we picked all the landward dipping thrusts and seaward dipping back-thrusts near the deformation front. The two examples in Fig. 9 illustrate how we picked these secondary faults. The time section of

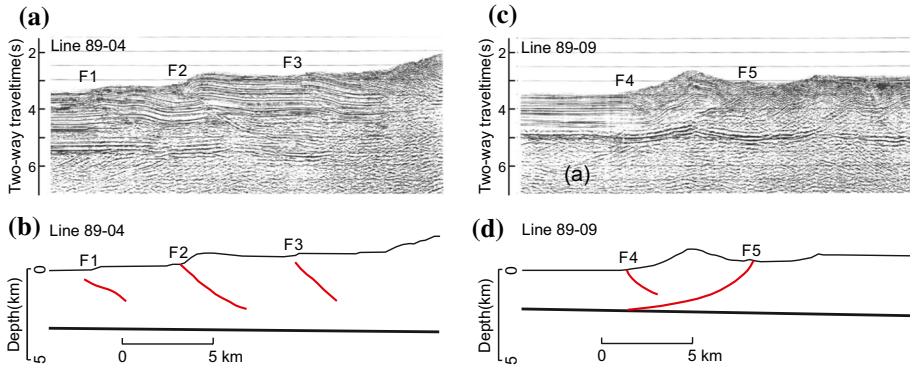


Fig. 9 Examples of potential tsunamigenic secondary faults near the deformation front identified from seismic imaging data. **a, c** Time sections of lines 89-04 and 89-09 (Hyndman et al. 1994), respectively. See Fig. 8 for locations. **b, d** Sketches of faults (red lines) identified in lines 89-04 and 89-09, respectively

Line 89-04 is shown in Fig. 9a, with its deformation structures sketched in the depth section shown in Fig. 9b. Three landward dipping thrusts (F1, F2, and F3) are present near the deformation front. F2 breaks the seafloor, but the other two do not seem to. It is difficult to tell whether these three thrusts penetrate to the top of the igneous oceanic crust because of limited data resolution. Neither is it known whether these faults would be activated seismically during previous great megathrust earthquakes or aseismically after or between great earthquakes. Line 89–09 shown in Fig. 9c (time section) and 9d (depth section) exhibits more complicated deformation in which both a thrust (F4) and a back-thrust (F5) are present in the sediment. A summary of identified secondary faults from the 10 seismic profiles are sketched in Fig. 10.

The incoming plate at northern Cascadia is blanketed by ~ 3 km of sediment near the deformation front. Off Vancouver Island, the deformation style of the sediment varies along the margin (Fig. 10). In a southern portion, there are multiple landward dipping thrusts. Half-way north the dip direction changes to being dominantly seaward (back-thrusting). Farther north, in the explorer segment, both seaward and landward dipping thrusts are present. If we map the seafloor locations of the dominant frontal thrusts and back-thrusts obtained from the seismic images onto the bathymetry map, it is clear that these locations correspond to tiny linear frontal anticlinal folds (Fig. 8). Therefore, individual frontal thrusts and back-thrusts offshore of Vancouver Island appear to be localized with very short strike lengths. Thus far, we have not been able to identify a geological structure that could indicate large trench-breaching seismic rupture in the past. Neither is there strong argument to exclude this possibility from past and future earthquakes. For tsunami hazard assessment, we need to construct a trench-breaching rupture model at least as a lower-probability scenario.

3.3.2 Models involving a hypothetical frontal thrust

In northern Cascadia, the décollement is near the base of the sediment section as suggested by Davis and Hyndman (1989). Because of the thick sediment cover, if a trench-breaching rupture does happen, it cannot happen in the manner portrayed by Fig. 1c. Instead, it has to be diverted from the megathrust to one of the frontal thrusts shown in Fig. 1d. Trench-breaching rupture may have limited strike lengths such as in the 2011 Tohoku-oki event,

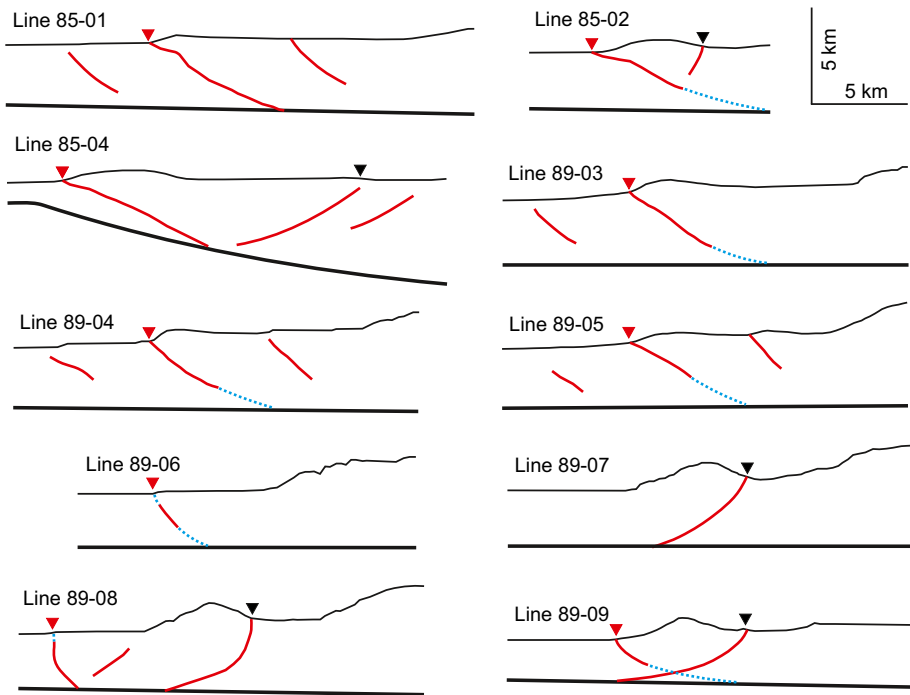


Fig. 10 Sketches of secondary faults (red lines) identified along ten of the seismic survey lines shown in Fig. 8. Red and black triangles denote inferred seafloor traces of dominant frontal thrusts and back-thrusts, respectively. Dashed blue lines show how coseismic slip along the megathrust may be diverted to the secondary faults

but a hypothetical model of frontal thrust that is continuous along strike is useful in representing a worst-case scenario of trench-breaching rupture (Fig. 8), although it is undoubtedly unrealistic.

To construct such a hypothetical frontal thrust model, we picked one dominant landward dipping thrust from each seismic profile (Fig. 10) (except Line 89-07 where no frontal thrust can be identified), assuming that the dominant thrust breaks the seafloor and soles into the décollement at a depth shallower than ~ 10 km below sea level. Taking Line 89-04 for example (Fig. 9a), F2 is the dominant thrust and breaches the seafloor. We assume F2 soles into the décollement along the dashed blue line shown in Fig. 10 and thus allow megathrust slip to be diverted to the frontal thrust up to the seafloor. Similar to the buried-rupture and splay-fault models (Figs. 4, 6) and as explained in Sect. 2.3, we consider three strike lengths of trench-breaching rupture (Table 1). The whole-margin trench-breaching rupture scenario is constructed by southward extrapolation of the hypothetical frontal thrust from northern Cascadia along the deformation front. The northern part of the whole-margin trench-breaching scenarios is shown in Fig. 11.

In the trench-breaching model, slip distribution in the downdip half of the rupture zone is exactly the same as that of the buried rupture, represented by the downdip half of the bell-shaped slip (Figs. 5, 12). Slip in the updip half is modelled using a segment of a sine function that allows the slip to decrease smoothly from the peak value in the middle of the rupture to a specified value at the seafloor trace of the frontal thrust. Like in Figs. 4, 5, 6, and 7, the peak value used for the models shown in Figs. 11 and 12 is that of 500 years of

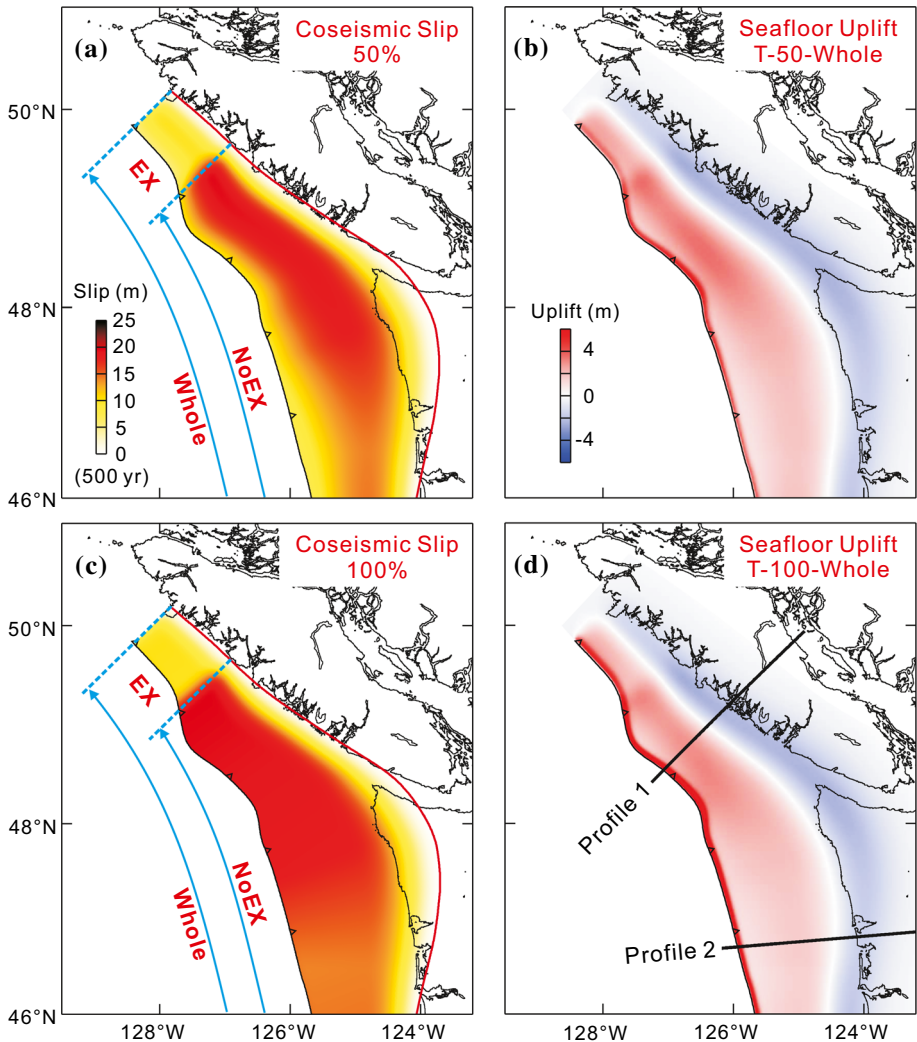


Fig. 11 Trench-breaching rupture scenarios (only north of 46°N is shown). The black barbed line marks the surface trace of the hypothetical frontal thrust which also defines the deformation front. Red solid line in the left-hand-side panels marks the downdip limit of coseismic slip. Segmentation in the strike direction is the same as in Fig. 4a. **a** Slip at fault trace = 50% of peak slip. **b** Seafloor uplift for model T-50-Whole. **c**, **d** Same as **a**, **b**, respectively, but for slip at fault trace = 100% of peak slip. Results along the two profiles are shown in Fig. 12

slip deficit. For demonstration purpose, slip at the seafloor trace is assumed to be 50% (T-50) or 100% (T-100) of the peak slip (see Table 1 and Fig. 12), but any other values can also be used. These different amounts of slip decrease in the updip direction crudely represent different degrees of coseismic strengthening (Hu and Wang 2008; Wang and He 2008) or dynamic weakening (Di Toro et al. 2011; Noda and Lapusta 2013; Sun et al. 2017) of the shallow portion of the megathrust. Greater slip at the seafloor means a lower

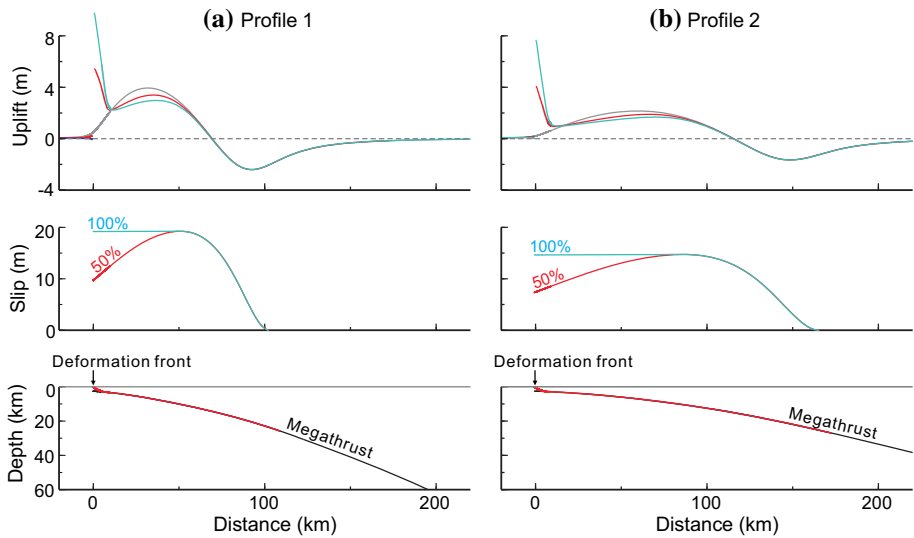


Fig. 12 Fault slip and surface deformation along the two profiles shown in Fig. 11. The two models (colour-coded solid lines) with different amounts of slip at the deformation front as fractions of the peak slip correspond to Fig. 11b, d. For each profile, the bottom panel shows the fault geometry with the red portion indicating the rupture zone, the middle panel shows fault slip distribution, and the upper panel shows seafloor uplift in comparison with that produced by the buried rupture (grey)

degree of coseismic strengthening to stop the rupture or a higher degree of dynamic weakening to facilitate rupture, and vice versa.

The contribution of a trench-breaching rupture to tsunami generation has two components. The first is the “rigid-body translation” component illustrated in the bottom panel of Fig. 3b, controlled mainly by the seafloor slope and fault dip. As explained in Sect. 2.2, this component is approximately accounted for in our flat-top dislocation model by the introduction of a fault dip adjustment (Fig. 3b). The other is the “deformation” component, that is, seafloor uplift or subsidence due to horizontal shortening and lengthening, respectively, of the upper plate material, controlled mainly by how the fault slip decreases or increases towards the trench. The deformation component may include some permanent deformation, but is modelled as purely elastic deformation in the dislocation model. The translation component is widely considered to have played an important role in generating the devastating tsunami during the 2011 Tohoku-oki earthquake (Figs. 1c, 3b). However, the translation component of the trench-breaching rupture at Cascadia may not be as effective in generating large tsunamis as in the Japan trench because the continental slope is not as steep, and the high-slope area is not as broad in the trench-normal direction.

By comparing Fig. 12 with Fig. 5, we expect a complex impact on tsunami generation by the deformation component of the trench-breaching rupture. Seafloor uplift is enhanced directly above the frontal thrust (Fig. 12) as compared to the buried-rupture model (Fig. 12), similar to the splay-fault model (Fig. 7) but with a much shorter wavelength. However, over the 10–60 km (Fig. 12a) or 80 km (Fig. 12b) distance range from the deformation front, seafloor uplift in both the trench-breaching models is less than that caused by the buried rupture, particularly along profile 1 where the megathrust dips more steeply (Fig. 12a). The greater the slip of the frontal thrust, the smaller the seafloor uplift in this area (Fig. 12). The smaller uplift here is the result of the less shortening of the upper

plate material due to the gentler or no decrease in fault slip towards the deformation front. The trade-off between the greater uplift over the frontal thrust and the less uplift farther landward is an important factor to consider in Cascadia trench-breaching rupture models. In Sect. 4, we will show an example of tsunami generation by these models using model T-100-Whole (Fig. 11d).

3.3.3 Other faulting scenarios near the deformation front

If the upper plate is shortened during an earthquake rupture because of trenchward decrease in slip magnitude, multiple thrusts and back-thrusts may be activated in megathrust earthquakes (Fig. 1d). It is very uncertain how much coseismic slip should be assigned to individual thrusts and back-thrusts. Besides, it would be impractical to design a model that features numerous juxtaposed small frontal thrust and back-thrust segments with very limited lengths in the strike direction. If such a complex rupture indeed occurs, we argue that the resultant seafloor uplift in a broad area can be approximated with elastic shortening due to a gentle slip decrease towards the trench, much like the scenarios shown in Fig. 11a. Effects of short-wavelength variations of the uplift caused by the motion of closely spaced individual thrusts will be smoothed out during tsunami propagation.

We also devised a hypothetical back-thrust geometrical model based on the seismic profiles (Lines 85-02, 85-04, 89-07, 89-08, and 89-09) shown in Fig. 10. Unlike frontal thrusts, back-thrusts do not act as a steeper continuation of the megathrust in seismic slip and are not very likely to have a large slip. We ran test models assuming slip equivalent to 50 and 100 years of plate convergence. The results, not displayed here, showed that back-thrust ruptures are unimportant for tsunami generation even if they were very long along strike (Gao 2016). The back-thrusts one could possibly infer from our seismic images would have rather short strike lengths (Gao 2016). Besides, we are not aware of any observation of significant back-thrust rupture contributing to tsunami generation in real megathrust earthquakes.

4 Applications to tsunami wave simulation

The coseismic deformation scenarios designed in the preceding section can be used as initial conditions for the simulation of tsunami generation and propagation for the purpose of tsunami hazard assessment or early warning. As examples, we display tsunami wave simulation results generated with scenarios B-Whole, S-A-Whole, and T-100-Whole for our region of interest. For the purpose of this work, we only display and discuss tsunami water surface elevation. These preliminary results are one step towards inundation models for more refined tsunami hazard assessment. Run-up heights would be much larger than the shown wave heights, and the actual values depend on site-specific conditions and should be numerically simulated with a more detailed digital elevation model and much finer model grid than used in this work. For illustration purpose and for the ease of comparison between models, we use 500-year slip deficit as the peak slip value in all the three models.

The tsunami simulation code employed in this study is FUNWAVE-TVD (Shi et al. 2016). It solves nonlinear and dispersive Boussinesq equations (Wei et al. 1995) for wave propagation in coastal areas and has been benchmarked against other tsunami simulation codes as part of the US National Tsunami Hazard Mitigation Program (Horrillo et al. 2015). FUNWAVE-TVD was run for this study in spherical coordinates with fully dispersive terms. The model uses a solver with adaptive Runge–Kutta time stepping. A fixed

bottom friction coefficient of 0.0025 was used in this study. Once wave breaking is detected, FUNWAVE-TVD switches from Boussinesq to Navier–Stokes wave equations which include breaking wave dissipation.

The vertical component of the coseismic surface deformation from our flat-top dislocation models is mapped to a digital elevation (bathymetry) grid for modelling tsunami generation and propagation. As pointed out by Lotto et al. (2017), kinetic energy imparted by horizontal velocities of the seafloor is unimportant in tsunami generation. The spherical earth modelling grid used for this study is referenced to the mean sea level with a horizontal resolution of 1 arcmin and is based on the ETOPO 1 global topography and bathymetry (Amante and Eakins 2009), the Canadian digital elevation model (CDEM) from the Government of Canada, and the British Columbia NOAA digital elevation model (DEM) (Carignan et al. 2013).

The focus of this paper is source definition, and the tsunami wave models are only meant to illustrate how different slip scenarios control the general pattern of tsunami waves. The results shown in this paper (Figs. 13, 14) are thus obtained with a coarse grid (1 arcmin horizontal resolution). Because of the aliasing effect of the coarse grid, wave heights at specific coastal locations may be underestimated. In particular, very short-wavelength tsunami waves likely generated by the splay-faulting and trench-breaching sources were probably not fully simulated. Even for the buried-rupture scenario, our numerical testing shows that a refined grid (15 arcsec) will predict higher water surface elevation maxima along the outer coast, although the overall pattern of the wave height distribution is the same as that obtained with the coarse grid (results not displayed). Therefore, the absolute values of the water surface elevation shown in Figs. 13 and 14 should not be taken at face value. It is the comparison of the general patterns and relative water elevation between different source models that is important. Tsunami models with a more detailed grid at a regional and coastal community level are out of the scope of this work and will be presented elsewhere (Insua et al., in preparation). We also plan to conduct numerical experiments to explore the effects of short-wavelength features of the splay-faulting and trench-breaching sources using more refined grids.

Figure 13 shows snapshots of simulated tsunami wave propagation for the buried-rupture scenario B-Whole, including the time the waves impact the coast (Fig. 4d). The coseismic seafloor deformation (Fig. 4b) is directly applied to the free sea water surface to act as initial conditions for tsunami wave propagation, featuring a positive peak far offshore and negative peak near the coast (Fig. 13a). Within a few minutes after the earthquake, the waves head seaward and landward (Fig. 13b). In less than half an hour, the landward propagating wave front reaches some coastal areas including the northern west coast of Vancouver Island (Fig. 13c). The wave front will become irregular when approaching the coast because of wave refraction, dispersion, and convergence due to bathymetrical variations along the shelf and coast as seen in earlier Cascadia tsunami models (Cherniawsky et al. 2007).

We have run similar simulations for the splay-faulting rupture S-A-Whole (Fig. 6b) and trench-breaching rupture T-100-Whole (Fig. 11d). Their spatiotemporal patterns of wave propagation (not displayed) are overall similar to those shown in Fig. 13, but with sharper wave fronts because of localized large coseismic seafloor uplift along the traces of the splay or frontal thrust (see Figs. 7, 12). We show the maximum sea surface elevations for a 10-h simulation after the earthquake for all the three models in Fig. 14. Interesting but of less importance is the pattern of outgoing waves into the Pacific: concave seaward shape of the megathrust source geometry causes focusing of energy seen as beaming of large wave heights.

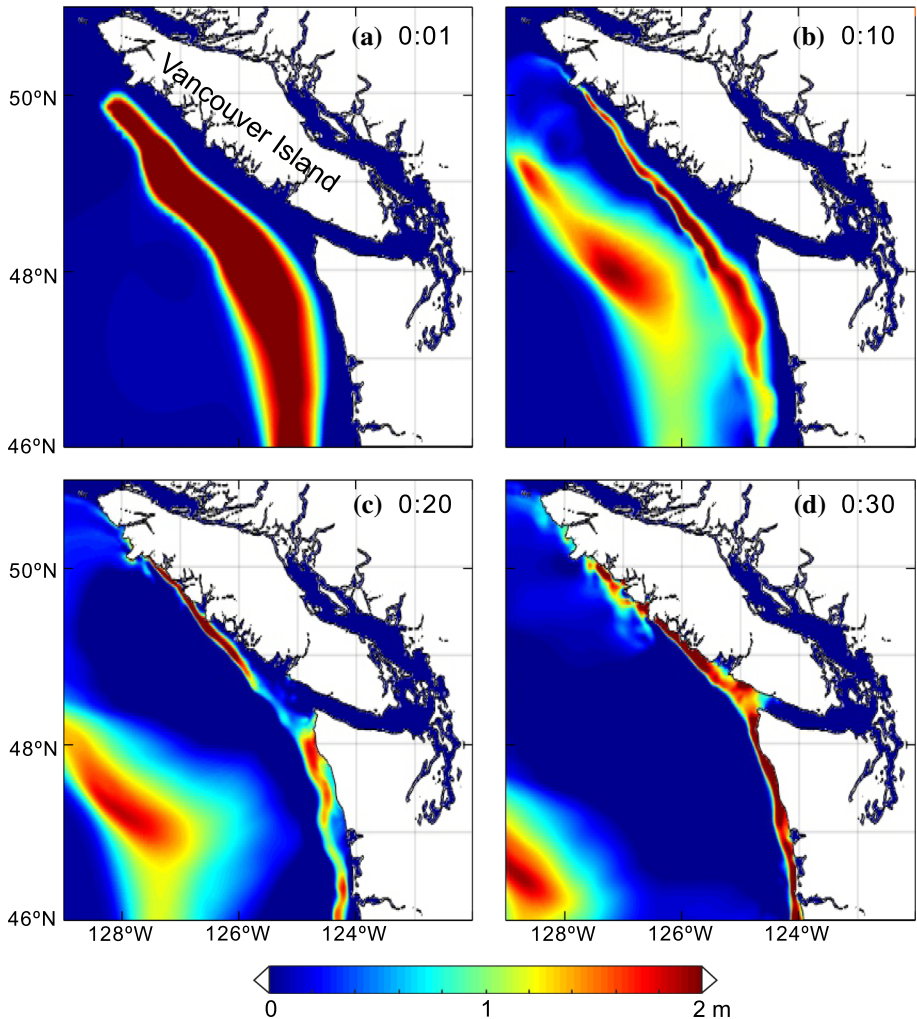


Fig. 13 Tsunami wave propagation model based on the whole-margin buried-rupture scenario B-Whole (see Table 1 and Fig. 4d). **a–d** are snapshots of water surface elevation (m) at 1, 10, 20, and 30 min after the earthquake, respectively. Height reference: North American Vertical Datum of 1988 (NAVD88) Mean Sea Level. Note that the colour scale saturates at both ends

Given the same peak fault slip, the splay-fault scenario features the highest tsunami waves everywhere along the coast (Fig. 14), the same as seen in previous Cascadia tsunami modelling work (Priest et al. 2010; Witter et al. 2013). The only exception is the northernmost area. Because the splay fault in model S-A-Whole does not extend that far north (Fig. 6a) and because of the short distance of the frontal thrust in T-100-Whole from the coast (Fig. 11c), the trench-breaching rupture causes slightly higher maximum water surface elevation off northern Vancouver Island (Fig. 14c).

As discussed in Sect. 3.3.2, compared with the buried-rupture model, seafloor uplift in the trench-breaching model is increased at the frontal thrust but decreased farther landward. The two opposite effects cause complex interactions of tsunami waves, and

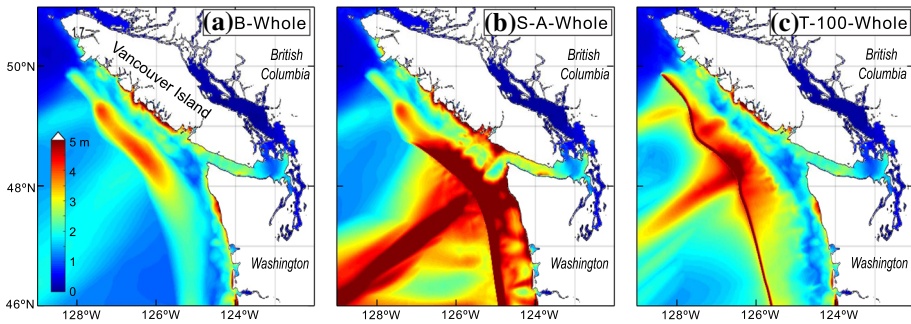


Fig. 14 Maximum water surface elevation during the first 10 h after the earthquake for three whole-margin megathrust rupture scenarios. Height reference: North American Vertical Datum of 1988 (NAVD88) Mean Sea Level. Note that the colour scale shown in **a** saturates at 5 m. See Table 1 for parameter definition. Peak fault slip in all the scenarios is equivalent to 500 years of slip deficit. **a** Buried-rupture scenario B-Whole (Fig. 4b). Snapshots of wave propagation are shown in Fig. 13. **b** Splay-fault scenario S-A-Whole (Fig. 6b). **c** Trench-breaching (frontal thrust) scenario T-100-Whole (Fig. 11d). Note that because of the coarse grid used for these illustration runs, near-shore maximum water surface elevation is under-predicted and should not be taken at face value

consequently the coastal wave elevation maxima (Fig. 14c) are in general slightly lower than the buried rupture (Fig. 14a). In T-100-Whole used here, the slip of the frontal thrust reaches 100% of the peak fault slip. Largely because of the reduced uplift over a broad area landward of the deformation front (Fig. 12b), tsunami wave heights generated by T-100-Whole (Fig. 14c) for most of the coastal areas are slightly lower than in the buried-rupture model (Fig. 14a). Wave heights in some places are larger because of the enhanced uplift over the frontal thrust, such as off northern Vancouver Island where the deformation front is close to the coast. We have also conducted tsunami simulation using T-50-Whole (50% peak slip) (results not displayed), and the resultant coastal wave heights are generally between those shown in Fig. 14a, c.

The very large slip at the deformation front as portrayed by T-100-Whole was seen in the Tohoku-oki earthquake, but may appear to be too dramatic for Cascadia, given the structural difference between the two margins (Fig. 1c, d). However, arguments can be made on the basis of seismically inferred mechanical strength of accretionary prism materials and weakness of the megathrust that very large coseismic slip may extend to the deformation front in central Cascadia (Han et al. 2017; Tobin and Webb 2017). Tsunami wave propagation models with finer numerical grids are needed for a better understanding of the wave dynamics and for addressing structural impact and hazardous currents generated by the tsunami waves.

5 Summary

This research addresses an urgent need in tsunami hazard assessment and risk mitigation at northernmost Cascadia. Given the acute shortage of geophysical and geological information to constrain the megathrust's rupture behaviour near the deformation front (Wang and Tréhu 2016), we have to make various assumptions on the basis of our current understanding of Cascadia's fault structure, knowledge of fault mechanics, and lessons learnt from recent large tsunamigenic earthquakes around the world. For the purpose of hazard assessment, assumed source scenarios should be embracive if not comprehensive. The

source scenarios presented in this paper serve to provide preliminary scientific basis for scenario-based probabilistic hazard assessment. Revising or refining these scenarios is an important task of future research. The main work we have done and what we have learnt are summarized as follows:

1. For developing tsunamigenic rupture scenarios, we have compiled a new megathrust geometry model for the Cascadia megathrust by smoothly connecting three parts (Fig. 2): the fault geometry of McCrory et al. (2012) for southern Cascadia, the geometry of McCrory et al. (2004) for northern and central Cascadia, and the geometry proposed by Gao et al. (2017) for northernmost Cascadia (the Explorer segment).
2. For tsunami hazard assessment at northernmost Cascadia, we have developed a suite of 15 tsunami source scenarios using a 3D dislocation model. The scenarios are of three categories: buried rupture, splay-faulting rupture, and trench-breaching rupture involving a hypothetical frontal thrust. All these source scenarios can result in large seafloor uplift and coastal subsidence and hence lead to tsunamis that seriously affect the coastal area. The models developed in this study did not consider short-wavelength along-strike fault slip variations. More realistic rupture scenarios should be investigated in the future.
3. The presence or absence of a dominant splay fault in northernmost Cascadia cannot be defined by the currently available seismic imaging data and geological knowledge. However, the impact of such a scenario on tsunami generation is very large, and its possibility cannot be excluded from hazard assessment. To account for this possibility, we have extrapolated the splay fault earlier assumed for Oregon and Washington to offshore of Vancouver Island with two possible scenarios (Figs. 6, 7).
4. An examination of marine multichannel seismic images with a focus on the accretionary wedge deformation front has not provided compelling evidence for trench-breaching ruptures during previous megathrust earthquakes at Cascadia, but this issue needs to be further investigated with high-resolution structural studies in the future. As a worse-case scenario of trench-breaching rupture, we have constructed a model involving a hypothetical frontal thrust that is continuous along strike (Fig. 11).
5. For illustration purpose, we show tsunami wave modelling results for one source model from each of the three categories of source scenarios, assuming a peak fault slip equivalent to 500 years of slip deficit. Given the same peak slip, the splay-fault model generates the highest tsunami waves along the coast, typically 50–100% higher than the buried rupture (Fig. 14). Compared to the buried rupture, frontal thrust rupture (up to 100% of peak slip) generally does not worsen tsunami hazard (Fig. 14), mainly because the effect of greater seafloor uplift over the frontal thrust is offset by reduced uplift farther landward. Our preliminary results indicate that the tsunami water surface elevation maxima are in general slightly lower than those of the buried rupture.

Acknowledgements We thank K. Rohr for assistance in interpreting seismic records for the identification of secondary faults shown in Fig. 10, S. Grilli and A. Grilli for help in wave propagation modelling, two anonymous reviewers for insightful comments, and Westgrid and compute Canada, in particular Dr. Belaid Moa, for their technical support on cloud and cluster computing. D. G., T. S., and M. S. were supported by a Natural Sciences and Engineering Council Canada (NSERC) Collaborative Research Grant (CRDPJ 492525-15) to K. W. and others for research collaboration with Ocean Networks Canada and IBM Canada and by an NSERC Discovery Grant to K. W. This is Geological Survey of Canada contribution 20180073.

References

- Allen TI, Hayes GP (2017) Alternative rupture-scaling relationships for subduction interface and other offshore environments. *Bull Seismol Soc Am* 107(3):1240–1253
- Amante C, Eakins BW (2009) ETOPO1 1 arc-minute global relief model: procedures, data sources and analysis. NOAA Technical Memorandum NESDIS NGDC-24
- Atwater BF, Nelson AR, Clague JJ, Carver GA, Yamaguchi DK, Bobrowsky PT, Bourgeois J, Darienzo ME, Grant WC, Hemphill-Haley E, Kelsey HM, Jacoby GC, Nishenko SP, Palmer SP, Peterson CD, Reinhart MA (1995) Summary of coastal geologic evidence for past great earthquakes at the Cascadia subduction zone. *Earthq spectra* 11(1):1–18
- Blaser L, Krüger F, Ohrnberger M, Scherbaum F (2010) Scaling relations of earthquake source parameter estimates with special focus on subduction environment. *Bull Seismol Soc Am* 100:2914–2926
- Carignan KS, Eakins BW, Love MR, Sutherland MG, McLean SJ (2013) Bathymetric digital elevation model of British Columbia, Canada: procedures, data sources, and analysis. Prepared for NOAA, Pacific Marine Environmental Laboratory (PMEL) by the NOAA National Geophysical Data Centre (NGDC)
- Cherniawsky JY, Titov VV, Wang K, Li JY (2007) Numerical simulations of tsunami waves and currents for southern Vancouver Island from a Cascadia megathrust earthquake. *Pure appl Geophys* 164(2–3):465–492
- Clowes RM, Yorath CJ, Hyndman RD (1987) Reflection mapping across the convergent margin of western Canada. *Geophys J Int* 89(1):79–84
- Cummins PR, Kaneda Y (2000) Possible splay fault slip during the 1946 Nankai earthquake. *Geophys Res Lett* 27(17):2725–2728
- Davis EE, Hyndman RD (1989) Accretion and recent deformation of sediments along the northern Cascadia subduction zone. *Geol Soc Am Bull* 101(11):1465–1480
- Di Toro G, Han R, Hirose T, De Paola N, Nielsen S, Mizoguchi K, Ferri F, Cocco M, Shimamoto T (2011) Fault lubrication during earthquakes. *Nature* 471(7339):494–498
- Flück P, Hyndman RD, Wang K (1997) Three-dimensional dislocation model for great earthquakes of the Cascadia subduction zone. *J Geophys Res: Sol Earth* 102(B9):20539–20550
- Fujiwara T, Kodaira S, Kaiho Y, Takahashi N, Kaneda Y (2011) The 2011 Tohoku-Oki earthquake: displacement reaching the trench axis. *Science* 334(6060):1240
- Gao D (2016) Defining megathrust tsunami sources at northernmost Cascadia using thermal and structural information. M.Sc. thesis, Univ. of Victoria, Victoria, BC, Canada
- Gao D, Wang K, Davis EE, Jiang Y, Insua TL, He J (2017) Thermal state of the explorer segment of the Cascadia subduction zone: implications for seismic and tsunami hazards. *Geochem Geophys Geosyst* 18(4):1569–1579
- Goldfinger C, Nelson CH, Morey AE, Johnson JE, Patton JR, Karabanov E, Gutierrez-Pastor J, Eriksson AT, Gracia E, Dunhill G, Enkin RJ (2012) Turbidite event history: Methods and implications for Holocene paleoseismicity of the Cascadia subduction zone. U.S. Geological Survey Professional Paper, 1661, 170
- Gulick SP, Austin JA Jr, McNeill LC, Bangs NL, Martin KM, Henstock TJ, Bull JM, Dean S, Djajadihardja YS, Permana H (2011) Updip rupture of the 2004 Sumatra earthquake extended by thick indurated sediments. *Nat Geosci* 4(7):453–456
- Han S, Bangs NL, Carbotte SM, Saffer DM, Gibson JC (2017) Links between sediment consolidation and Cascadia megathrust slip behavior. *Nat Geosci* 10(12):954–959. <https://doi.org/10.1038/s41561-017-0007-2>
- Hanks TC, Kanamori H (1979) A moment magnitude scale. *J Geophys Res* 84:2348–2350
- Henstock TJ, McNeill LC, Tappin DR (2006) Seafloor morphology of the Sumatran subduction zone: surface rupture during megathrust earthquakes? *Geology* 34(6):485–488
- Horrillo J, Grilli ST, Nicolisky D, Roeber V, Zhang J (2015) Performance benchmarking tsunami models for NTHMP's inundation mapping activities. *Pure appl Geophys* 172(3–4):869–884
- Hsu YJ, Simons M, Avouac JP, Galetzka J, Sieh K, Chlieh M, Natawidirdjo D, Prawirodirdjo L, Bock Y (2006) Frictional afterslip following the 2005 Nias-Simeulue earthquake. *Sumatra Sci* 312(5782):1921–1926
- Hu Y, Wang K (2008) Coseismic strengthening of the shallow portion of the subduction fault and its effects on wedge taper. *J Geophys Res: Sol Earth* 113:B12411
- Hyndman RD, Spence GD, Yuan T, Davis EE (1994) 10. Regional geophysics and structural framework of the Vancouver Island accretionary prism. In: Proceedings of the ocean drilling program, initial reports, 146(1)

- Kodaira S, No T, Nakamura Y, Fujiwara T, Kaiho Y, Miura S, Takahashi N, Kaneda Y, Taira A (2012) Coseismic fault rupture at the trench axis during the 2011 Tohoku-Oki earthquake. *Nat Geosci* 5(9):646–650
- Leonard LJ, Rogers GC, Mazzotti S (2012) A preliminary tsunami hazard assessment of the Canadian coastline. Geological Survey of Canada, Open File 7201:126
- Lotto GC, Nava G, Dunham EM (2017) Should tsunami simulations include a nonzero initial horizontal velocity? *Earth Planet Sp* 69:117
- Ludwin RS, Dennis R, Carver D, McMillan AD, Losey R, Clague J, Jonientz-Trisler C, Bowe chop J, Wray J, James K (2005) Dating the 1700 Cascadia earthquake: great coastal earthquakes in native stories. *Seismol Res Lett* 76(2):140–148
- McCrory PA, Blair JL, Oppenheimer DH, Walter SR (2004) Depth to the Juan de Fuca slab beneath the Cascadia subduction margin: A 3-D model for sorting earthquakes. US Department of the Interior, US Geological Survey
- McCrory PA, Blair JL, Waldhauser F, Oppenheimer DH (2012) Juan de Fuca slab geometry and its relation to Wadati-Benioff zone seismicity. *J Geophys Res: Sol Earth* 117:B09306
- Moeremans R, Singh SC, Mukti M, McArdle J, Johansen K (2014) Seismic images of structural variations along the deformation front of the Andaman–Sumatra subduction zone: implications for rupture propagation and tsunamigenesis. *Earth Planet Sci Lett* 386:75–85
- Murotani S, Satake K, Fujii Y (2013) Scaling relations of seismic moment, rupture area, average slip, and asperity size for $M \sim 9$ subduction-zone earthquakes. *Geophys Res Lett* 40:5070–5074
- Noda H, Lapusta N (2013) Stable creeping fault segments can become destructive as a result of dynamic weakening. *Nature* 493(7433):518–521
- Okada Y (1985) Surface deformation due to shear and tensile faults in a half-space. *Bull Seismol Soc Am* 75(4):1135–1154
- Okada Y (1992) Internal deformation due to shear and tensile faults in a half-space. *Bull Seismol Soc Am* 82(2):1018–1040.
- Priest GR, Witter RC, Zhang YJ, Wang K, Goldfinger C, Stimely LL, English JT, Pickner, SG, Hughes KLB, Wille TE, Smith RL (2013) Tsunami inundation scenarios for Oregon. Oregon Department of Geology and Mineral Industries, Open-file report 0-13-19
- Plafker G (1972) Alaskan earthquake of 1964 and Chilean earthquake of 1960: implications for arc tectonics. *J Geophys Res* 77(5):901–925
- Priest GR, Goldfinger C, Wang K, Witter RC, Zhang Y, Baptista AM (2009) Tsunami hazard assessment of the Northern Oregon coast: a multi-deterministic approach tested at Cannon Beach, Clatsop County, Oregon. Oregon Department of Geology and Mineral Industries, Special Paper 41
- Priest GR, Goldfinger C, Wang K, Witter RC, Zhang Y, Baptista AM (2010) Confidence levels for tsunami-inundation limits in northern Oregon inferred from a 10,000-year history of great earthquakes at the Cascadia subduction zone. *Nat Hazard* 54(1):27–73
- Priest GR, Zhang Y, Witter RC, Wang K, Goldfinger C, Stimely L (2014) Tsunami impact to Washington and northern Oregon from segment ruptures on the southern Cascadia subduction zone. *Nat Hazard* 72(2):849–870
- Royer AA, Bostock MG (2014) A comparative study of low frequency earthquake templates in northern Cascadia. *Earth Planet Sci Lett* 402:247–256
- Satake K, Wang K, Atwater BF (2003) Fault slip and seismic moment of the 1700 Cascadia earthquake inferred from Japanese tsunami descriptions. *J Geophys Res: Sol Earth* 108:2535
- Shi F, Kirby JT, Tehranirad B, Harris JC, Choi Y-K, Malej M (2016) FUNWAVE-TVD, Fully Nonlinear Boussinesq Wave Model With TVD solver, documentation and user's manual. Center Appl. Coastal Res., Univ. Delaware, Newark, DE, USA, Res. Rep. No CACR-11-04
- Singh SC, Carton H, Taponnier P, Hananto ND, Chauhan AP, Hartoyo D, Bayly M, Moeljoproanto S, Bunting T, Christie P, Lubis H, Martin J (2008) Seismic evidence for broken oceanic crust in the 2004 Sumatra earthquake epicentral region. *Nat Geosci* 1(11):777–781
- Singh SC, Hananto N, Mukti M, Permana H, Djajadihardja Y, Harjono H (2011) Seismic images of the megathrust rupture during the 25th October 2010 Pagai earthquake, SW Sumatra: frontal rupture and large tsunami. *Geophys Res Lett* 38(16)
- Spence GD, Hyndman RD, Davis EE, Yorath CJ (1991a) Seismic structure of the northern Cascadia accretionary prism: evidence from new multichannel seismic reflection data. *Continental Lithosphere: Deep Seismic Reflections*, 257-263
- Spence GD, Hyndman RD, Langton S, Yorath CJ, Davis EE (1991b) Multichannel seismic reflection profiles across the Vancouver Island continental shelf and slope. *Geol Surv Can Open File*, 2391
- Strasser FO, Arango MC, Bommer JJ (2010) Scaling of the source dimensions of interface and intraslab subduction-zone earthquakes with moment magnitude. *Seismol Res Lett* 81:941–950

- Sun T, Wang K (2015) Viscoelastic relaxation following subduction earthquakes and its effects on afterslip determination. *J Geophys Res Sol Earth* 120(2):1329–1344
- Sun T, Wang K, Fujiwara T, Kodaira S, He J (2017) Large fault slip peaking at trench in the 2011 Tohoku-oki earthquake. *Nat Commun* 8:14044
- Tobin HJ, Webb SI (2017) Evidence for patchy sediment underthrusting and a strong, drained outer accretionary wedge in central Cascadia: implications for dynamic slip conditions. American Geophysical Union Fall Meeting, December 2017, Abstract T43F-07
- Wang PL (2012) Rupture models of the great 1700 Cascadia earthquake based on microfossil paleoseismic observations. M.Sc. thesis, Univ of Victoria, Victoria, BC, Canada
- Wang K, He J (2008) Effects of frictional behaviour and geometry of subduction fault on coseismic seafloor deformation. *Bull Seismol Soc Am* 98(2):571–579
- Wang K, Hu Y (2006) Accretionary prisms in subduction earthquake cycles: the theory of dynamic Coulomb wedge. *J Geophys Res Sol Earth* 111:B06410
- Wang K, Tréhu AM (2016) Invited review paper: some outstanding issues in the study of great megathrust earthquakes—The Cascadia example. *J Geodyn* 98:1–18
- Wang K, Wells R, Mazzotti S, Hyndman RD, Sagiya T (2003) A revised dislocation model of interseismic deformation of the Cascadia subduction zone. *J Geophys Res Sol Earth* 108:2026
- Wang PL, Engelhart SE, Wang K, Hawkes AD, Horton BP, Nelson AR, Witter RC (2013) Heterogeneous rupture in the great Cascadia earthquake of 1700 inferred from coastal subsidence estimates. *J Geophys Res Sol Earth* 118(5):2460–2473
- Wang K, Sun T, Brown L, Hino R, Tomita M, Kido M, Inuma T, Kodaira S, Fujiwara T (2018) Learning from crustal deformation associated with the M9 2011 Tohoku-oki earthquake. *Geosphere*. <https://doi.org/10.1130/GES01531.1>
- Wei G, Kirby JT, Grilli ST, Subramanya R (1995) A fully nonlinear Boussinesq model for surface waves. Part 1. Highly nonlinear unsteady waves. *J Fluid Mech* 294:71–92
- Wells DL, Coppersmith KJ (1994) New empirical relationships among magnitude, rupture length, rupture width, rupture area, and surface displacement. *Bull Seismol Soc Am* 84:974–1002
- Wells RE, Simpson RW (2001) Northward migration of the Cascadia forearc in the northwestern U.S. and implications for subduction deformation. *Earth Planet Sp* 53:275–283
- Wendt J, Oglesby DD, Geist EL (2009) Tsunamis and splay fault dynamics. *Geophys Res Lett*. <https://doi.org/10.1029/2009GL038295>
- Witter RC, Zhang Y, Wang K, Priest GR, Goldfinger C, Stimely LL, English JT, Ferro PA (2011) Simulating tsunami inundation at Bandon, Coos County, Oregon, using hypothetical Cascadia and Alaska earthquake scenarios. Oregon Department of Geology and Mineral Industries Special Paper 43
- Witter RC, Zhang Y, Wang K, Goldfinger C, Priest GR, Allan JC (2012) Coseismic slip on the southern Cascadia megathrust implied by tsunami deposits in an Oregon lake and earthquake triggered marine turbidites. *J Geophys Res: Sol Earth* 117:B10303
- Witter RC, Zhang YJ, Wang K, Priest GR, Goldfinger C, Stimely L, English JT, Ferro PA (2013) Simulated tsunami inundation for a range of Cascadia megathrust earthquake scenarios at Bandon, Oregon, USA. *Geosphere* 9(6):1783–1803
- Yorath CJ, Clowes RM, MacDonald RD, Spencer C, Davis EE, Hyndman RD, Rohr K, Sweeny JF, Currie RG, Halpen JF, Halpenny JF, Seemann DA (1987) Marine multichannel seismic reflection, gravity and magnetic profiles: Vancouver Island continental margin and Juan de Fuca ridge. Geological Survey of Canada, Open file, 1661
- Yuan T, Spence GD, Hyndman RD (1994) Seismic velocities and inferred porosities in the accretionary wedge sediments at the Cascadia margin. *J Geophys Res Sol Earth* 99(B3):4413–4427